Supplementary Materials

Defective graphene synergizes with NiO_x nanosheets to facilitate dual-defect-assisted two-electron oxygen reduction

Run Huang[1], Helong Wu[1], Qingchao Fang[2], Ying Chen[1], Panjie Guo[1], Xuan Liu[1], Mengting Huang[1], Jinyan Zhang[1], Aijun Du[2], Lei Wang[1,*], Xin Wang[1,*]

[1]College of Chemical Engineering, Zhejiang University of Technology, Hangzhou 310032, Zhejiang, China.
[2]School of Chemistry, Physics and Mechanical Engineering Queensland University of Technology Brisbane, Brisbane 4000, Australia.

[*]**Correspondence to:** Prof. Lei Wang, Prof. Xin Wang, College of Chemical Engineering, Zhejiang University of Technology, Hangzhou 310032, Zhejiang, China. E-mail: sumin224@zjut.edu.cn; wangxin136@zjut.edu.cn

1. DFT Calculation

Spin-polarized density function theory (DFT) was conducted using the Vienna ab initio Simulation Package (VASP).[1] The plane-wave cutoff energy is set to 500 eV. The interactions between ions and electrons were described by projector-augmented wave (PAW) pseudopotentials.[2] The generalized gradient approximation (GGA) functional in the form of Perdew, Burke, and Ernzerhof (PBE) was used to estimate the exchange-correlation effects.[3, 4] The van der Waals interactions were considered using Grimme's DFT-D3 dispersion correction.[5] The Brillouin zone was sampled with the 3 X 3 X 1 Monkhorst-Pack k-points grids. The convergence criteria for total energy and residual force were set to be 10^{-5} eV and 0.01 eV/Å, respectively. GGA + U method was incorporated for the electron localisation on Ni 3d electrons with U of 6.4 eV.[6] To eliminate the interactions between adjacent layers, a vacuum region of 20 Å was created along the z axis. To study the influence of defect effect on the reaction, three NiO/graphene heterojunction composites with O or C defects were built with a mismatch tolerance of 4.4%. To assess the catalytic activity for oxygen reduction reaction (ORR), the two-electron reduction scheme was chosen. The Gibbs free energy of elementary reactions was calculated as follows:

$$\Delta G_i = \Delta E_{DFT} + \Delta ZPE - T\Delta S - eU - k_B T ln10 * pH$$

where ΔE_{DFT} is the energy from DFT calculations, ΔZPE and $T\Delta S$ are the variations in the zero-point energy and entropy, respectively. T is the temperature. U is the electrode potential and e is the electron transfer. k_B is the Boltzmann's constant.

2. Supplementary Figures

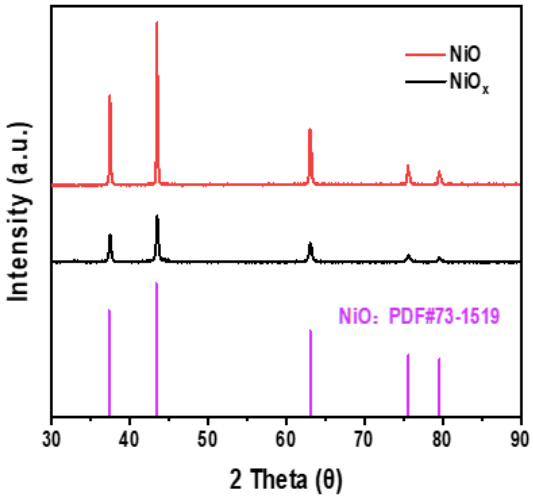

Supplementary Figure 1. XRD spectra of NiO_x powder.

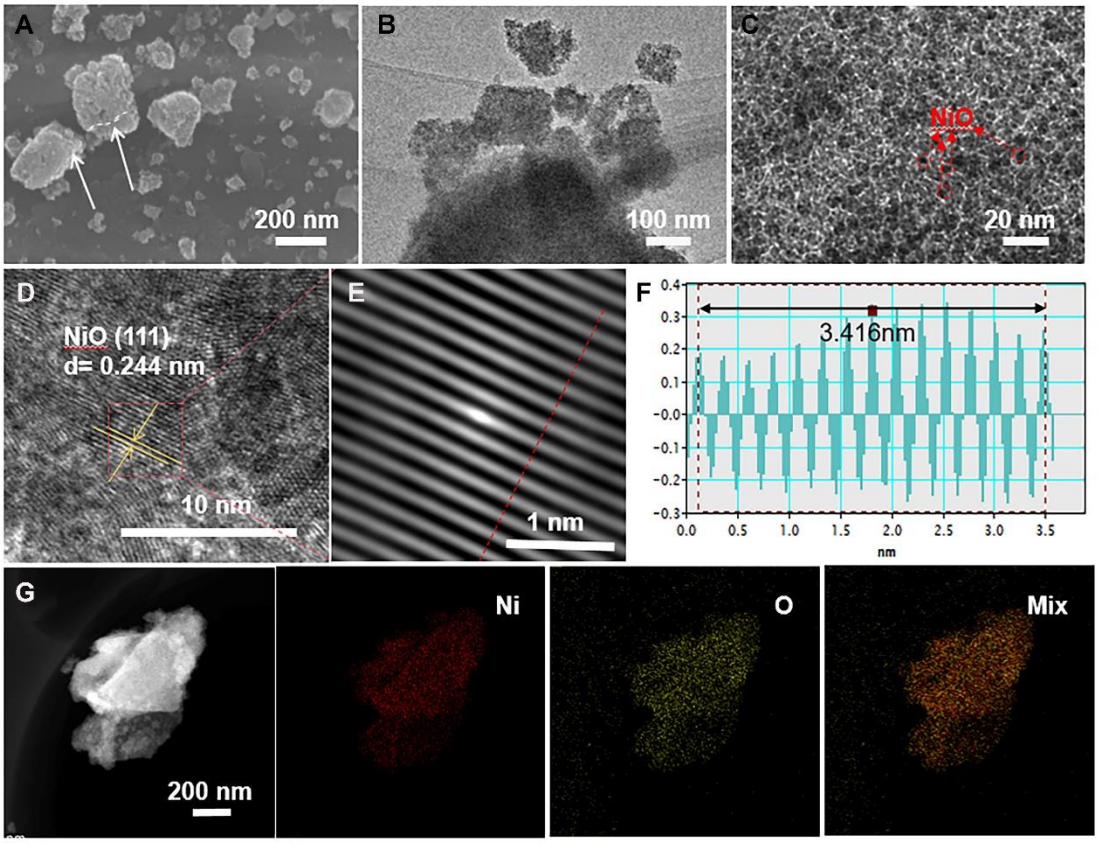

Supplementary Figure 2. (A) SEM image, (B) TEM image, (C) and (D) HRTEM images and (E) corresponding IFFT images of NiO_x nanosheet. (F) The corresponding lattice spacing image. (G) Elemental mapping spectra of NiO_x nanosheets.

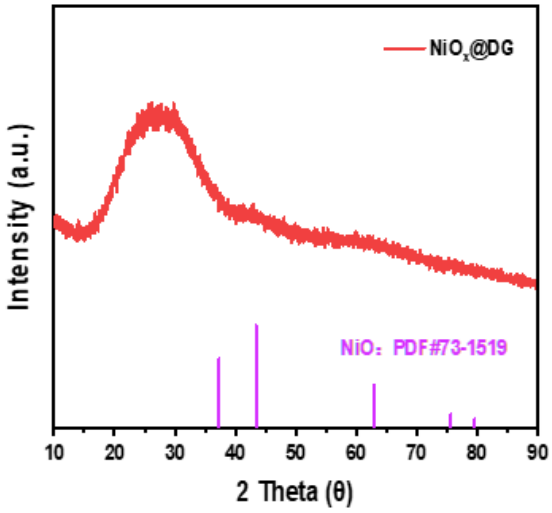

Supplementary Figure 3. XRD spectra of NiO_x@DG. Due to the low content of NiO_x nanosheets after centrifugation, it is difficult to detect. Therefore, we use a catalyst after hydrothermal recombination for XRD testing.

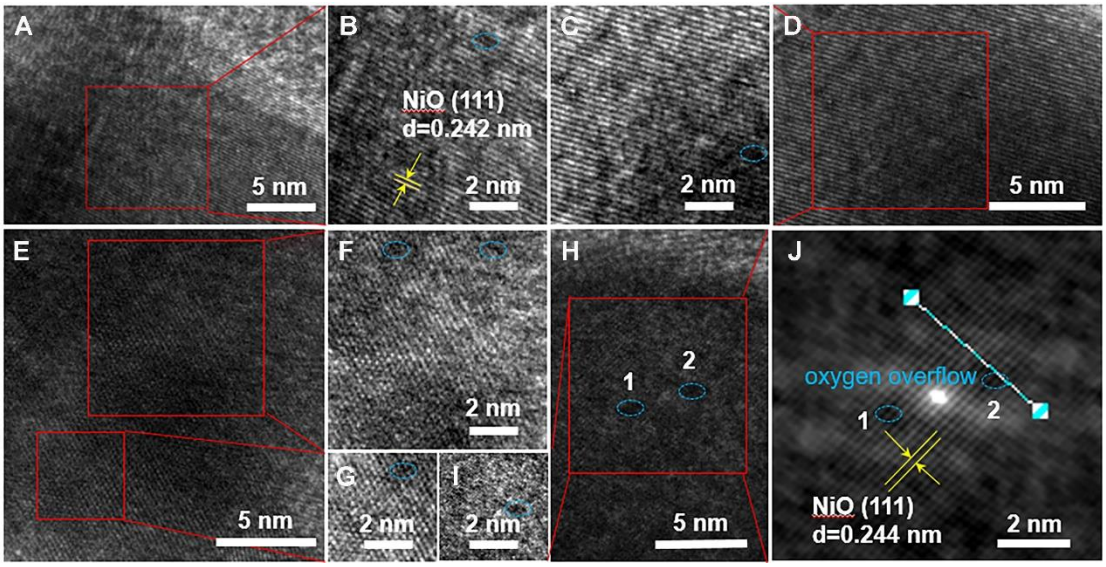

Supplementary Figure 4. (A, D, E and H) HRTEM images of NiO_x@DG. (B, C, F, G, I and J) The enlarged HRTEM images within the red dashed frame marks the local area of disordered atoms.

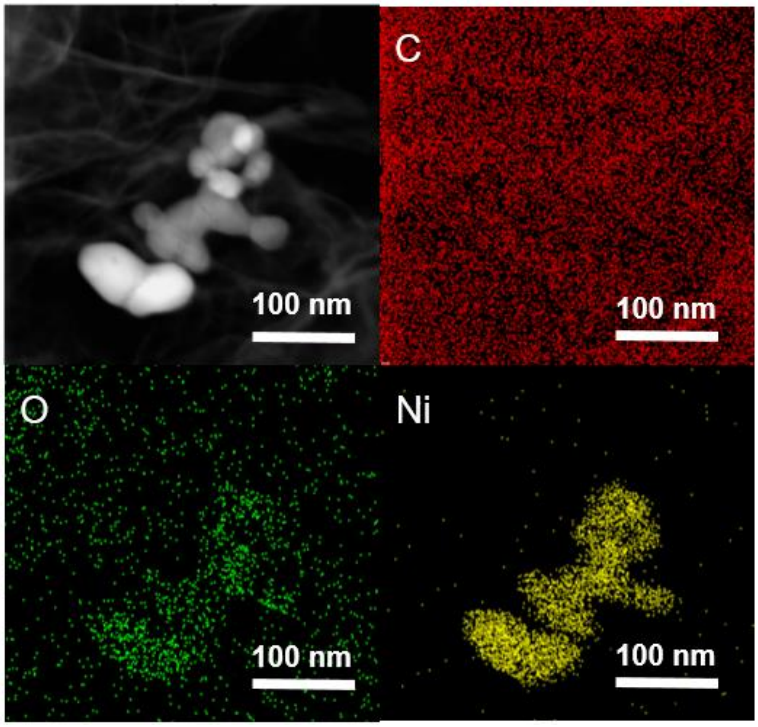

Supplementary Figure 5. EDS elemental mapping spectra of C, O and Ni over the NiO_x@DG.

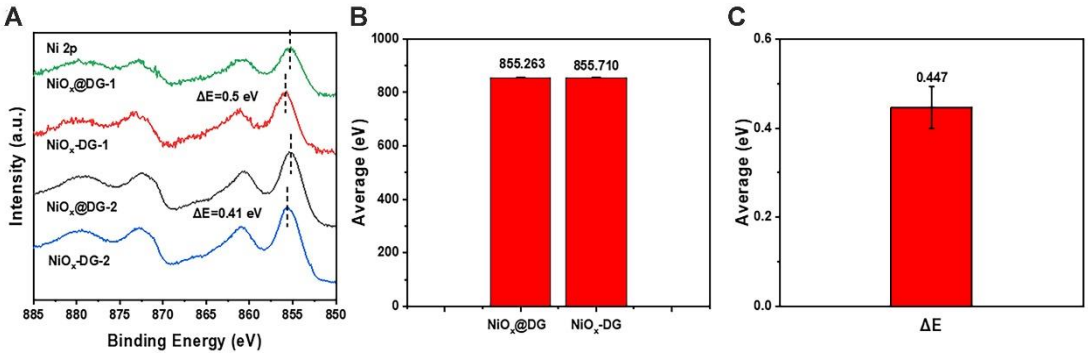

Supplementary Figure 6. (A) Multiple Ni 2p XPS tests for NiO_x@DG and NiO_x-DG; (B) Average binding energy of NiO_x@DG and NiO_x-DG; (C) Average value of the shifted binding energy. Among them, the error bars in (B) represent the binding energy errors of the NiO_x@DG sample measured three times, and those in (C) represent the errors of its shift (ΔE).

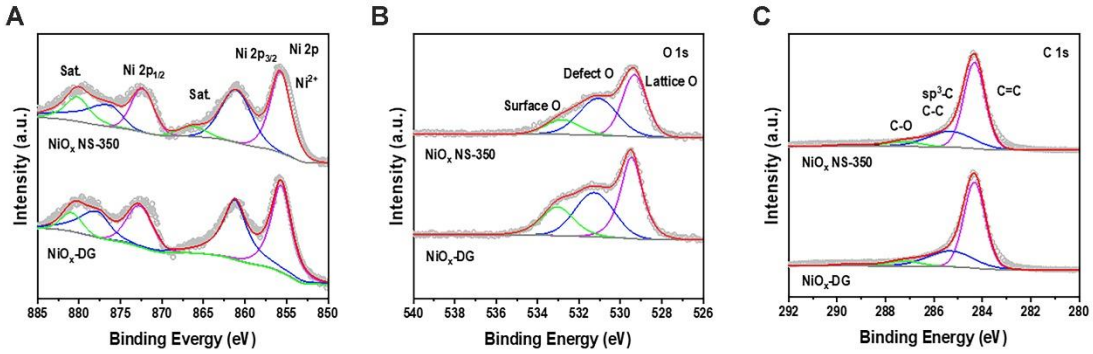

Supplementary Figure 7. Deconvoluted XPS spectra of NiO_x NS-350 and NiO_x-DG for (A) Ni 2p, (B) O 1s, (C) C 1s.

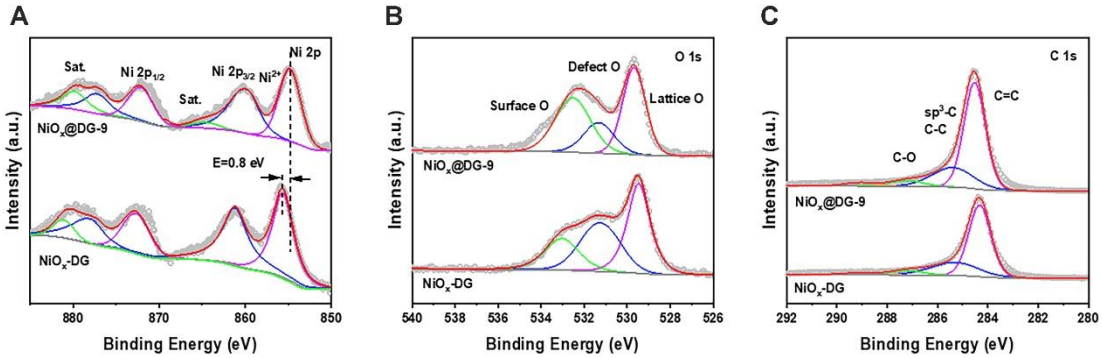

Supplementary Figure 8. Deconvoluted XPS spectra of NiO_x@DG-9 and NiO_x-DG for (A) Ni 2p, (B) O 1s, (C) C 1s.

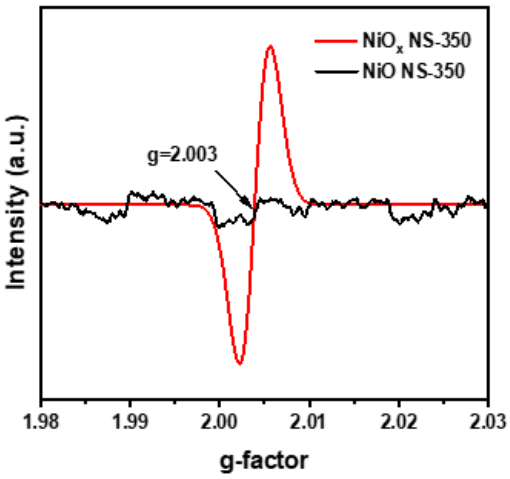

Supplementary Figure 9. EPR spectra of NiO_x NS-350 and NiO NS-350.

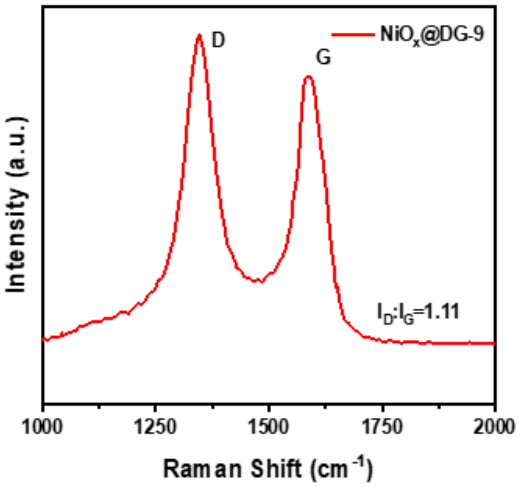

Supplementary Figure 10. Raman spectra of NiO_x@DG-9.

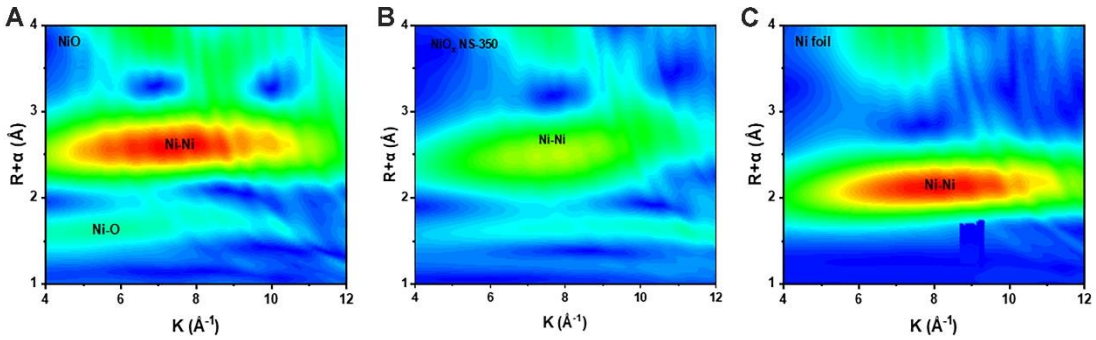

Supplementary Figure 11. Wavelet transforms of the EXAFS spectra of (A) NiO, (B) NiO_x NS-350 and (C) Ni foil.

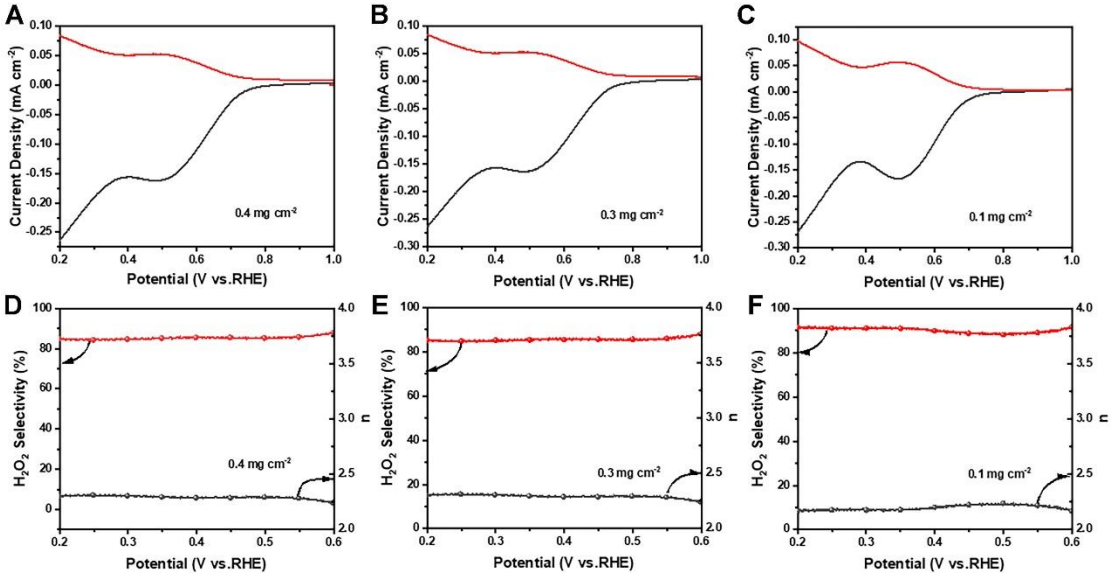

Supplementary Figure 12. LSV polarization curves with different loading amounts. (A-C) Polarization curves with different loading amounts (0.4 mg cm^{-2}, 0.3 mg cm^{-2}

and 0.1mg cm^{-2}) on RRDE at 1600 rpm in O_2-saturated 0.1 M KOH; (D-F) The corresponding calculated H_2O_2 selectivity and transfer electron number (n).

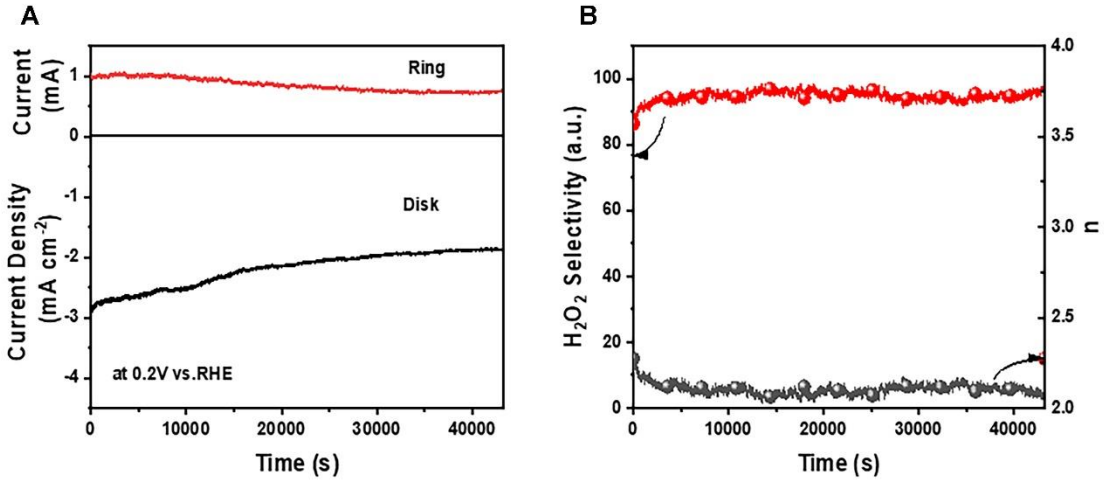

Supplementary Figure 13. (A) Chronoamperometry stability test of NiO_x@DG at 0.2 V vs. RHE in O_2-saturated 0.1 M KOH; (B) The calculated H_2O_2 selectivity and transfer electron number (n) of catalysts.

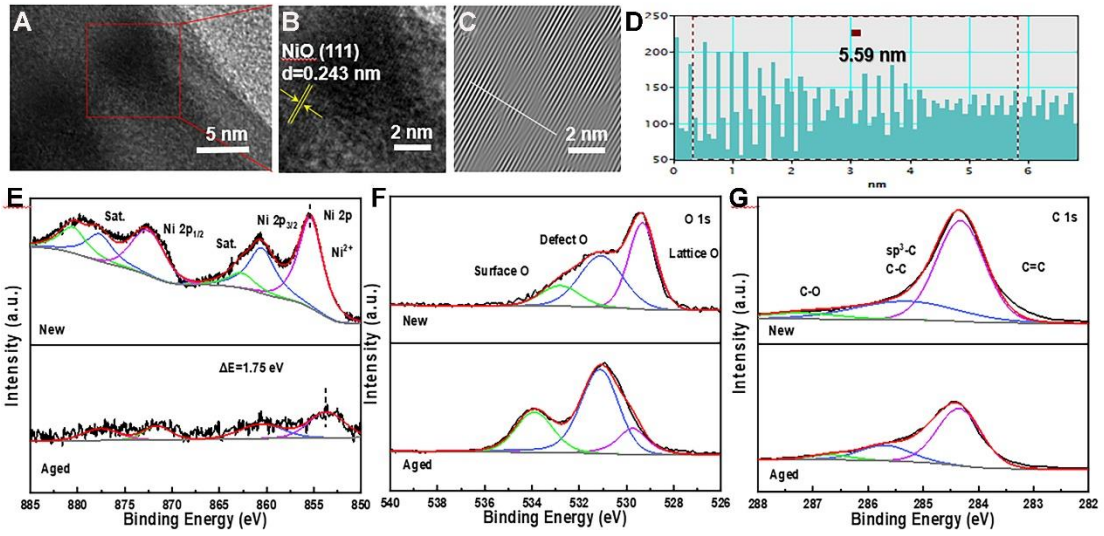

Supplementary Figure 14. (A and B) HRTEM image and (C) The enlarged HRTEM image within the red dashed frame marks the local area of disordered atoms. (D) Lattice spacing diagram. (E-G) Ni 2p, O1s and C1s XPS spectra before and after the stability test for NiO_x@DG catalyst.

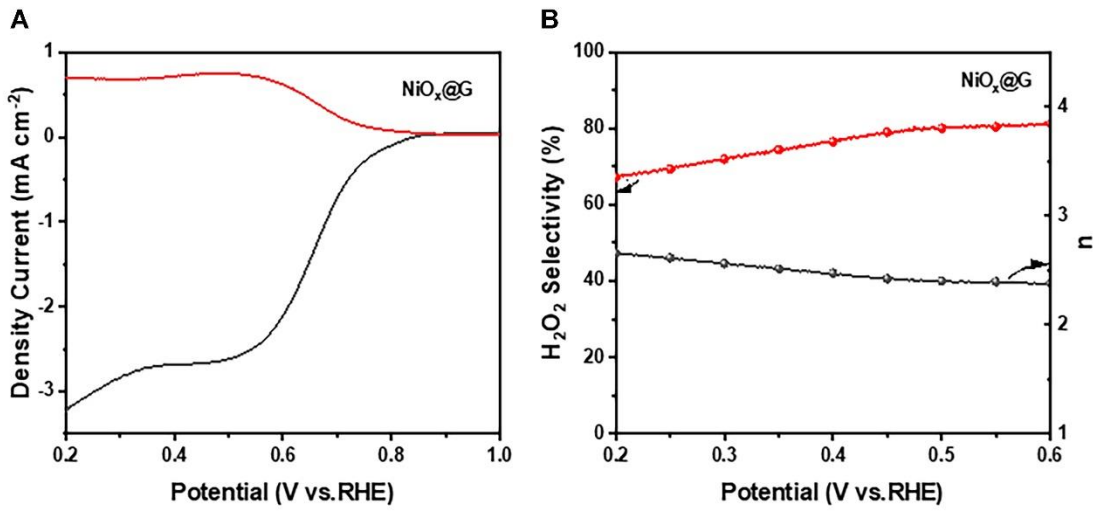

Supplementary Figure 15. (A) Polarization curves of NiO_x@G on RRDE at 1,600 rpm in O_2-saturated 0.1 M KOH; (B) The calculated H_2O_2 selectivity and transfer electron number (n) of catalysts.

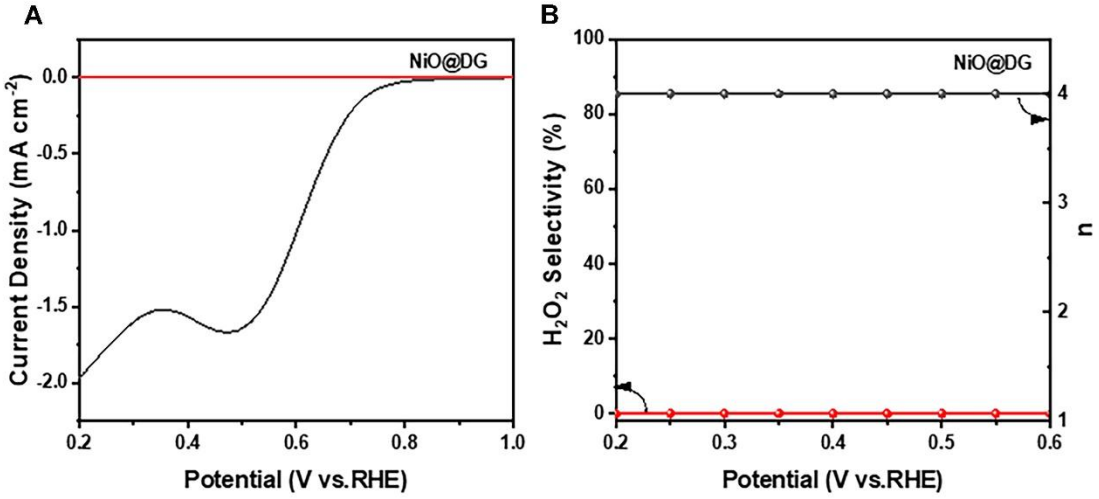

Supplementary Figure 16. (A) Polarization curves of NiO@DG on RRDE at 1,600 rpm in O_2-saturated 0.1 M KOH; (B) The calculated H_2O_2 selectivity and Transfer electron number (n) of catalysts.

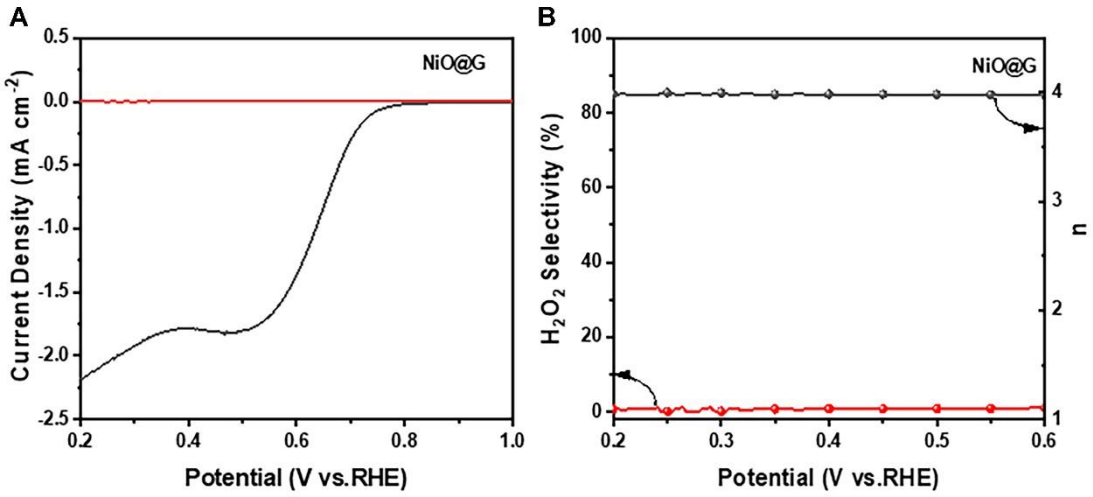

Supplementary Figure 17. (A) Polarization curves of NiO@G on RRDE at 1,600 rpm in O_2-saturated 0.1 M KOH; (B) The calculated H_2O_2 selectivity and Transfer electron number (n) of catalysts.

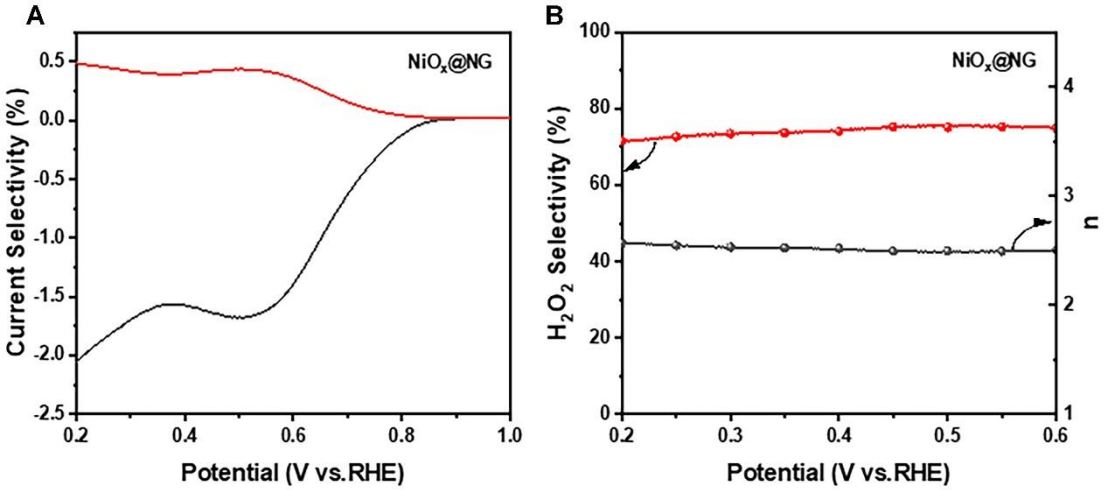

Supplementary Figure 18. (A) Polarization curves of NiO_x@NG on RRDE at 1,600 rpm in O_2-saturated 0.1 M KOH; (B) The calculated H_2O_2 selectivity and Transfer electron number (n) of catalysts.

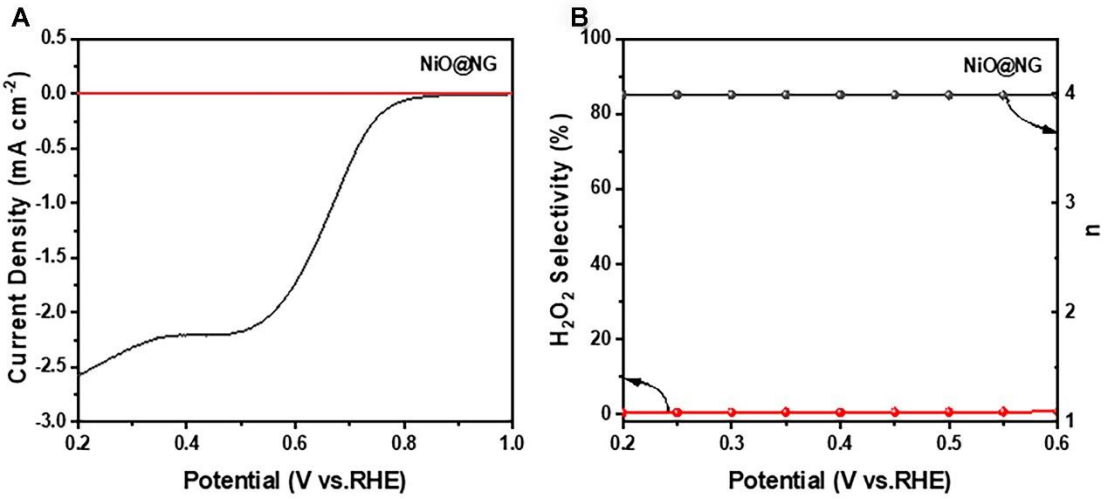

Supplementary Figure 19. (A) Polarization curves of NiO@NG on RRDE at 1,600 rpm in O_2-saturated 0.1 M KOH; (B) The calculated H_2O_2 selectivity and Transfer electron number (n) of catalysts.

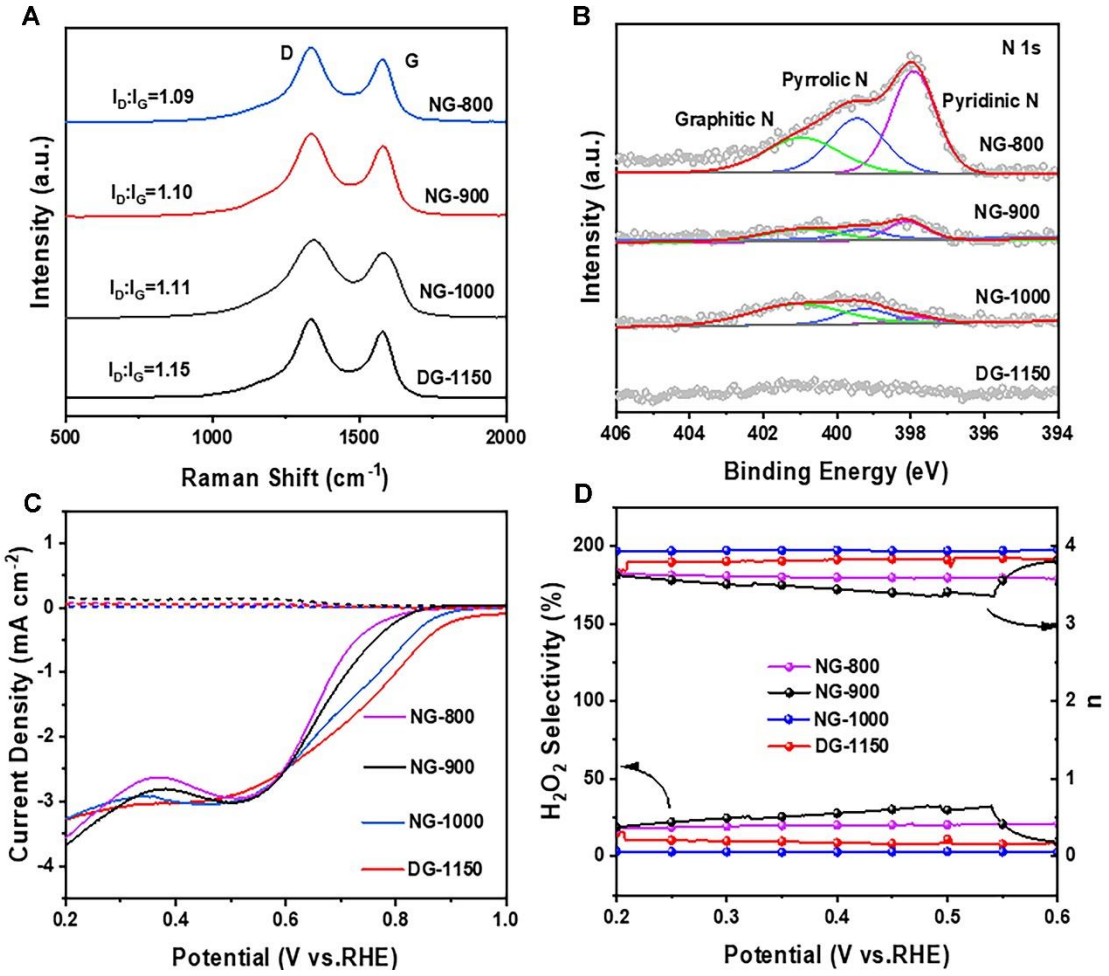

Supplementary Figure 20. (A) Raman spectroscopy of NG-800, NG-900, NG-1000 and DG-1150; (B) N 1s XPS spectra of NG-800, NG-900, NG-1000 and DG-1150;

(C) Polarization curves of NG-800, NG-900, NG-1000 and DG-1150; (D) The calculated H_2O_2 selectivity and Transfer electron number (n) of NG-800, NG-900, NG-1000 and DG-1150.

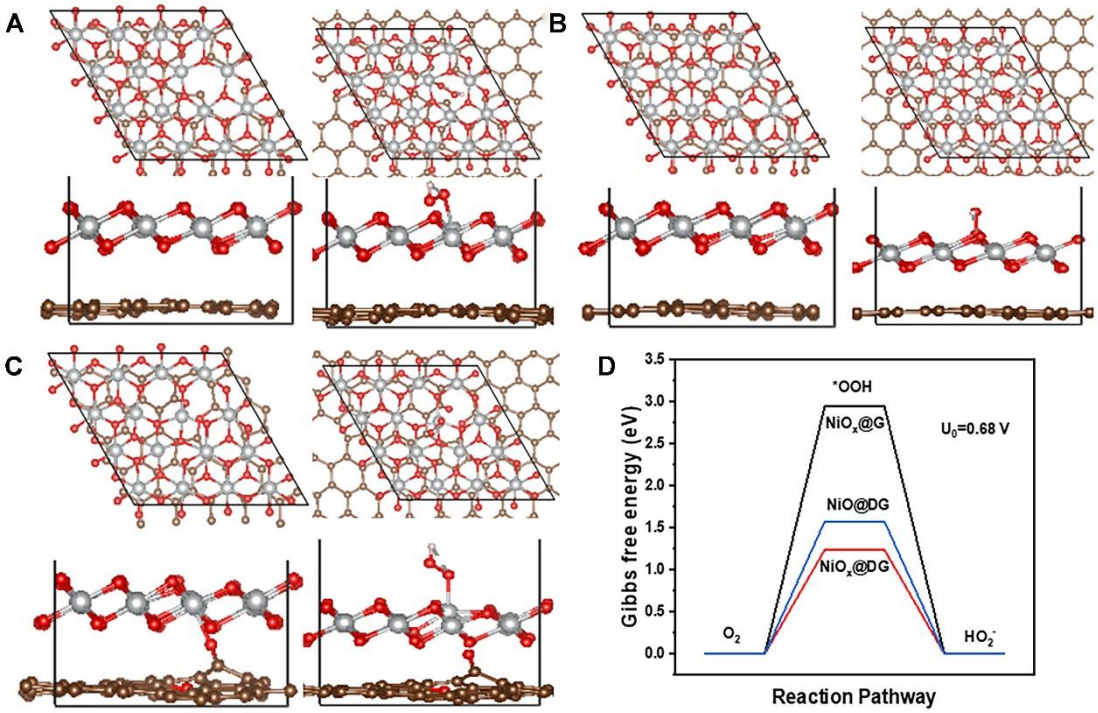

Supplementary Figure 21. DFT calculation results. (A) The theoretical model of NiO_x@DG and its *OOH adsorption configuration, top and side views; (B) The theoretical model of NiO_x@G and its *OOH adsorption configuration, top and side views; (C) The theoretical model of NiO@DG and its *OOH adsorption configuration, top and side views. Red represents O, brown represents C, and gray represents Ni; (D) Gibbs free energy plot of oxygen reduction to HO_2^- at pH = 13.0.

Supplementary Table 1. EXAFS fitting parameters at the Ni K-edge for NiO_x@DG. (S_0^2 = 0.75)

Sample	Path	CN	R(Å)	σ^2 (Å^2)	R-factor
NiO_x@DG	Ni-O	4.46	2.08±0.013	0.0057	0.01

CN: Coordination Number; R: Bond Distance; σ^2: Debye-Waller Factor; R-factor: Fit Goodness. According to the experimental EXAFS fitting of the nickel foil referenced in the literature, the CN is fixed at the known crystallographic value, and S_0^2 is the amplitude reduction factor, which is set to 0.75 here.

Supplementary Table 2. List of previously reported catalysts for hydrogen peroxide (H_2O_2) production

Catalyst	H_2O_2 Selectivity	Catalyst Loading	Operating Conditions	References
NiO_x@DG	~95%	0.2 mg cm^{-2}	0.1M KOH	This work
Ni_{SA}/Ni_{NP}-NSCNT	92.7~98.8 % 0.2 to 0.6 V vs.RHE	0.2 mg cm^{-2}	0.1M KOH	[15]
OCG800	92~100 % 0.05 to 0.7 V vs.RHE	0.78 mg cm^{-2}	H-cell, 0.1 M KOH + 10 mM EDTA, 0.4 V vs.RHE	[16]
O-CNTs	90 % at 0.65 V(vs.RHE)	0.5 mg cm^{-2}	0.1 M KOH	[17]
Co_1-NG(O)	82 %	10 μg cm^{-2}	0.1 M KOH	[18]
Co-SAs/CN	76 % at 0.65 V vs.RHE	/	0.1 M KOH	[19]
Pt-SA/rGO	60 % at 0.4 V vs.RHE	101.8 μg cm^{-2}	0.1 M KOH	[20]
Ni-SA/G-0	100 % at 0.4 V vs.RHE	50.8 μg cm^{-2}	0.1 M KOH	[21]
CB-Plasma	~100 %	16 μg cm^{-2}	0.1 M KOH	[22]

OCB120-CTAB	95.2 % at 0.5 V vs.RHE	/	0.1 M KOH	[23]
Br-Ni MOF	88.6 % at 0.4 V vs.RHE	50 ul (73mg/L)	0.1 M KOH	[24]
COF-366-Co	90 %	5 μg cm^{-2}	0.1 M KOH	[25]
Meso-C	80 % at 0.4 V vs.RHE	0.51 mg cm^{-2}	0.1 M KOH	[26]

Supplementary Table 3. Comparison of stability results between our catalyst and previously reported materials

Catalyst	**H_2O_2 Selectivity**	**Time**	**Potential**	**References**
NiO_x@DG	86%-96%	12 h	0.2 V vs.RHE	This work
OCG-800	~100%	10h	0.65 V vs.RHE	[16]
XGnP (X: I ,Br, Cl)	85.6–87.4%	10000s	-0.25 V vs. Ag/AgCl	[7]
Mn CD/C	/	10h	0.5 V vs.RHE	[27]

Supplementary Table 4. Inductively coupled plasma massspectrometry (ICP-MS) results for electrolytes after CV stability testing

Sample	**Sample volume V(mL)**	**Test elements**	**Test solution element concentration C_0(ug/L)**	**Elemental concentration of the original solution of the digestion solution C_1 (ug/L)**	**Sample elemental content C_x(ug/L)**
electrolyte	2	Ni	1.23676959072717	1.23676959072717	6.18
electrolyte	2	Ni	1.23333451563844	1.23333451563844	6.17
electrolyte	2	Ni	1.25089852200608	1.25089852200608	6.25

electrolyte	2	Pt	Not detected	Not detected	Not detected
electrolyte	2	Pt	Not detected	Not detected	Not detected
electrolyte	2	Pt	Not detected	Not detected	Not detected

In the table above, C_0: the concentration of elements in the test solution, unit: ug/L, the data is obtained by instrument testing; C_1: Element concentration of the sample digest stock solution, unit: ug/L, C_1(ug/L)=C_0(ug/L)*f, f=1; C_x: final test result of the measured element, unit: ug/L.

REFERENCES

1.Kresse, G., Furthmüller, J. Efficient iterative schemes for ab initio total-energy calculations using a plane-wave basis set. *Phys. Rev. B.* **1996;** *54*, 11169-11186. https://doi.org/10.1103/PhysRevB.54.11169

2.Blöchl, P. E. Projector augmented-wave method. *Phys. Rev. B.* **1994;** *50*, 17953-17979. https://doi.org/10.1103/PhysRevB.50.17953

3.Perdew, J. P.; Chevary, J. A.; Vosko, S. H., et al. Atoms, molecules, solids, and surfaces: Applications of the generalized gradient approximation for exchange and correlation. *Phys. Rev. B* **1992;** *46*, 6671-6687. https://doi.org/10.1103/PhysRevB.46.6671

4.Perdew, J. P., Wang, Y. Accurate and simple analytic representation of the electron-gas correlation energy. *Phys. Rev. B.* **1992;** *45*, 13244-13249. https://doi.org/10.1103/PhysRevB.45.13244

5.Grimme, S. Semiempirical GGA-type density functional constructed with a long-range dispersion correction. *J. Comput. Chem.* **2006;** *27*, 1787-1799. https://doi.org/10.1002/jcc.20495

6.Wang, L.; Maxisch, T., Ceder, G. Oxidation energies of transition metal oxides within the GGA+ U framework. *Phys. Rev. B-Condens Matter.* **2006;** *73*, 195107. https://doi.org/10.1103/PhysRevB.73.195107.

7.Jeon, I. Y.; Choi, H. J.; Choi, M., et al. Facile, scalable synthesis of edge-halogenated graphene nanoplatelets as efficient metal-free eletrocatalysts for oxygen reduction reaction. *Sci. Rep.* **2013;** *3*, 1810. https://doi.org/10.1038/srep01810

8.Zhang, C.; Shen, W.; Guo, K.; Xiong, M.; Zhang, J., Lu, X. A Pentagonal Defect-Rich Metal-Free Carbon Electrocatalyst for Boosting Acidic O_2 Reduction to H_2O_2 Production. *J. Am. Chem. Soc.* **2023;** *145*, 11589-11598. https://doi.org/10.1021/jacs.3c00689
9.Wu, Q.; Zou, H.; Mao, X., et al. Unveiling the dynamic active site of defective carbon-based electrocatalysts for hydrogen peroxide production. *Nat. Commun.* **2023;** *14*, 6275. https://doi.org/10.1038/s41467-023-41947-7
10.Cao, P.; Zhao, X.; Liu, Y., et al. Highly Efficient Acidic Electrosynthesis of Hydrogen Peroxide at Industrial-Level Current Densities Promoted by Alkali Metal Cations. *Angew. Chem. Int. Ed. Engl.* **2024;** *63*, e202406452. https://doi.org/10.1002/anie.202406452
11.Li, H.; Kelly, S.; Guevarra, D., et al. Analysis of the limitations in the oxygen reduction activity of transition metal oxide surfaces. *Nat. Catal.* **2021;** *4*, 463-468. https://doi.org/10.1038/s41929-021-00618-w
12.Yu, L.; Sun, S.; Li, H., Xu, Z. J. Effects of catalyst mass loading on electrocatalytic activity: An example of oxygen evolution reaction. *Fundamental Res.* **2021;** *1*, 448-452. https://doi.org/10.1016/j.fmre.2021.06.006
13.Lin, R.; Kang, L.; Lisowska, K., et al. Approaching Theoretical Performances of Electrocatalytic Hydrogen Peroxide Generation by Cobalt-Nitrogen Moieties. *Angew. Chem. Int. Ed. Engl.* **2023;** *62*, e202301433. https://doi.org/10.1002/anie.202301433
14.Wu, Z.; Wang, T.; Zou, J.-J.; Li, Y., Zhang, C. Amorphous Nickel Oxides Supported on Carbon Nanosheets as High-Performance Catalysts for Electrochemical Synthesis of Hydrogen Peroxide. *ACS Catal.* **2022;** *12*, 5911-5920. 10.1021/acscatal.2c01829
15.Wang, X.; Huang, R.; Mao, X., et al. Coupling Ni Single Atomic Sites with Metallic Aggregates at Adjacent Geometry on Carbon Support for Efficient Hydrogen Peroxide Electrosynthesis. *Adv. Sci.* **2024;** *11*, 2402240. https://doi.org/10.1002/advs.202402240
16.Lee, K.; Lim, J.; Lee, M. J., et al. Structure-controlled graphene electrocatalysts for high-performance H_2O_2 production. *Energy & Environ. Sci.* **2022;** *15*, 2858-2866. https://doi.org/10.1039/d2ee00548d
17.Lu, Z.; Chen, G.; Siahrostami, S., et al. High-efficiency oxygen reduction to hydrogen peroxide catalysed by oxidized carbon materials. *Nat. Catal.* **2018;** *1*, 156-162. https://doi.org/10.1038/s41929-017-0017-x

18.Jung, E.; Shin, H.; Hooch Antink, W.; Sung, Y.-E., Hyeon, T. Recent Advances in Electrochemical Oxygen Reduction to H_2O_2: Catalyst and Cell Design. *ACS Energy Lett.* **2020;** *5*, 1881-1892. https://doi.org/10.1021/acsenergylett.0c00812
19.Xu, H.; Zhang, S.; Geng, J.; Wang, G., Zhang, H. Cobalt single atom catalysts for the efficient electrosynthesis of hydrogen peroxide. *Inorg. Chem. Front.* **2021;** *8*, 2829-2834. https://doi.org/10.1039/D1QI00158B
20.Song, X.; Li, N.; Zhang, H.; Wang, H.; Wang, L., Bian, Z. Promotion of hydrogen peroxide production on graphene-supported atomically dispersed platinum: Effects of size on oxygen reduction reaction pathway. *J. Power Sources* **2019;** *435*, 226771. https://doi.org/10.1016/j.jpowsour.2019.226771
21.Song, X.; Li, N.; Zhang, H., et al. Graphene-Supported Single Nickel Atom Catalyst for Highly Selective and Efficient Hydrogen Peroxide Production. *ACS Appl. Mater. Interfaces* **2020;** *12*, 17519-17527. 10.1021/acsami.0c01278
22.Wang, Z.; Li, Q.-K.; Zhang, C., et al. Hydrogen Peroxide Generation with 100% Faradaic Efficiency on Metal-Free Carbon Black. *ACS Catal.* **2021;** *11*, 2454-2459. https://doi.org/10.1021/acscatal.0c04735
23.Wu, K.-H.; Wang, D.; Lu, X., et al. Highly Selective Hydrogen Peroxide Electrosynthesis on Carbon: In Situ Interface Engineering with Surfactants. *Chem* **2020;** *6*, 1443-1458. https://doi.org/10.1016/j.chempr.2020.04.002
24.Liu, M.; Li, Y.; Qi, Z., et al. Self-Nanocavity-Confined Halogen Anions Boosting the High Selectivity of the Two-Electron Oxygen Reduction Pathway over Ni-Based MOFs. *J. Phys. Chem. Lett.* **2021;** *12*, 8706-8712. https://doi.org/10.1021/acs.jpclett.1c01981
25.Liu, C.; Li, H.; Liu, F., et al. Intrinsic Activity of Metal Centers in Metal–Nitrogen–Carbon Single-Atom Catalysts for Hydrogen Peroxide Synthesis. *J. Am. Chem. Soc.* **2020;** *142*, 21861-21871. https://doi.org/10.1021/jacs.0c10636
26.Chen, S.; Chen, Z.; Siahrostami, S., et al. Defective Carbon-Based Materials for the Electrochemical Synthesis of Hydrogen Peroxide. *ACS Sustain. Chem. Eng.* **2017;** *6*, 311-317. https://doi.org/10.1021/acssuschemeng.7b02517
27.Zeng, Y.; Tan, X.; Zhuang, Z.; Chen, C., Peng, Q. Nature-Inspired N, O Co-Coordinated Manganese Single-Atom Catalyst for Efficient Hydrogen Peroxide Electrosynthesis. *Angew. Chem. Int. Ed. Engl.* **2024**, e202416715. 10.1002/anie.202416715